Electronic Supplementary Material (ESI) for Journal of Materials Chemistry A.


# Electronic Supplementary Information for

# Optimized Contact in Membrane Electrode Assembly for Multicarbon Products Generation

Tengfei Ma,‡[a] Haoran Qiu,‡[a] Wenhao Jing,[a] Feng Wang,[a] Ya Liu,*[a] and Liejin Guo*[a]

[a] International Research Center for Renewable Energy, State Key Laboratory of Multiphase Flow in Power Engineering, Xi'an Jiaotong University, Shaanxi 710049, China.

‡ These authors contributed equally to this work.

* Authors to whom correspondence should be addressed: yaliu0112@mail.xjtu.edu.cn and lj-guo@mail.xjtu.edu.cn

## Experimental section

**Materials**

Cu target (99.99%), hydrochloric acid (HCl), absolute ethanol (EtOH), iridium chloride hydrate ($IrCl_3 \cdot xH_2O$, Ir>52%), titanium mesh (100 mesh), nickel foam (thickness: 1.6 mm, bulk density: 0.45 g $cm^{-3}$), nickel mesh (100 mesh), potassium hydroxide (KOH).

**Preparation of electrodes**

***Fabrication of Cu electrode***

This work used the Polytetrafluoroethylene (PTFE) gas diffusion layer (GDL) as the cathode substrate. Cu was sputtered onto the substrate using pure Cu (99.99%) as a target. The sputtering was carried out under 5E–3 with a 25 nm $min^{-1}$ yield at room temperature.

***Fabrication of NiFe LDH/NF and NiFe LDH/NN***

The anode was synthesized via a typical electrodeposition.[1] Nickel foam and net were washed with 5 M HCl solution to remove the oxide layer on the surface, and then rinsed using a standard procedure with water and ethanol, and finally dried in air. The electrodeposition was carried out in a three-electrode cell in 3mM $Ni(NO_3)_2$ and 3mM $Fe(NO_3)_3$, with NF and NN serving as the working electrode, while platinum and Ag/AgCl acted as the reference electrode and counter electrode, respectively. The electrolyte was put in a breaker bathing in water to maintain 10 °C. The electrodeposition was carried out at –1 V (vs Ag/AgCl) for 300 s, then the electrodes were washed with deionized water and sonicated briefly in ethanol, and dried in air.

***Fabrication of $IrO_x$/Ti***

The $IrO_x$ on titanium (0.23 mm thickness, 100 mesh) was prepared by dipping coating and thermal decomposition method.[2] Briefly, the Ti mesh was washed using a standard procedure and etched in 6 M HCl solution heated at 85 °C for 45 min before dip coating. The dip coating solution consists of 60 mg $IrCl_3 \cdot xH_2O$ (Ir > 52%), 9 ml isopropanol, and 1 ml concentrated HCl. Then the etched Ti mesh was dipped into the solution. Before calcination in the furnace at 500 °C for 10 min, it was dried in an oven at 100 °C. The loading (1mg $cm^{-2}$) was achieved by repeating the dip and calcination.

**Characterization**

X-ray diffraction (XRD) patterns of electrode surface were confirmed by an X'Pert PRO diffractometer using Cu Kα (λ = 0.1538 nm) irradiation with constant instrument parameters. All the samples were scanned between 10° and 90° with a step size of 0.05° 2θ. Surface morphology characterization was performed by a JEOL JSM–7800F field emission scanning electron microscope (FE–SEM), and energy dispersive X-ray spectroscopy (EDS) analysis was conducted using the installed energy-dispersive X-ray detector, OXFORD INCA. X-ray photoelectron spectroscopy (XPS) measurements were done using a Kratos

spectrometer (Axis UltraDLD) with monochromatic Al Kα radiation (*hv* = 1486.69 eV). The C 1s signal centered at 284.8 eV, adventitious carbon, was used to calibrate the binding energies. The contact points and cross-sectional images were obtained using a camera mounted on DCAT 25 and a metallographic microscope.

**Electrochemical performance**

The $CO_2$RR experiments were performed using a custom-made membrane electrode assembly (MEA) (shown in Figure S10). The anode is grade 2 titanium, cathode is 904 L stainless steel. A peek gasket was put between the anode and cathode plate to act as an insulator. The copper tape which controls the reaction area and is wider than the O-ring, was lasered to 1 $cm^2$ in the center. Kapton tape was touched to the inviscid face of copper tape before lasered. The cathode and anode were at two sides of the ion exchange membrane (Sustainion X 37-50) which was immersed in 1 M KOH for 24 h before being mounted to the electrolyzer. Before being fed into the cathode, $CO_2$ was set to 30 sccm by a mass flow controller to saturate the humidifier with 25 ml deionized water for at least 30 min. A peristaltic pump was used to make sure electrolyte was fed to anode flow with 1 mL $min^{-1}$ and collected in a glass tube. The volume of collected products-containing electrolytes was obtained by mearing the weight of the glass tube before and after the test. The electrolyte was firstly deionized water pumped to anode for 3 min then changed to 1 M KOH. Two pieces of heater connected to a temperature controller were attached to the outside of the reactor to heat it for 5 min before the test to maintain 50 °C. The measurement was conducted using the Galvanostic model. The time of the applied current is set to 30 minutes. The overpotentials of prepared anode electrodes were measured via linear sweep voltammetry (LSV) as well as Cu cathode in a flow cell in 1 M KOH. The scanning rate of LSV was set at 10 mV $s^{-1}$. Electrochemical impendence spectroscopy (EIS) was carried out from 100K Hz to 0.1 Hz.

**Products analysis**

The gas products after $CO_2$ reduction were token from the cold trap after the cathode outlet at least 15 min of cell operation at a constant current. A mass flow meter continuously records the flow rates of the cathode outlet. Flow rates are using the average flow rates one minute before and after the 15th minute. Gas products were analyzed by gas chromatography from Agilent (7890) with a thermal conductivity detector (TCD). The liquid products include two parts, one part in a cold trap bathing in water 0 °C in the cathode outlet and one part in the electrolyte of the anode outlet. All liquid products were analyzed by high-performance liquid chromatography (1260 Infinity II LC System, Agilent Technologies, Inc, Santa Clara, CA, USA) with a refractive index detector (RID) and a column (Aminex HPX 87-H, Bio-Rad Laboratories, Inc., Hercules, CA, USA) from Bio-Rad. A total of 10 mM diluted sulfuric acid was used as the eluent, and 10 μL of the sample was injected into the column.

**Faradaic efficiency (FE) and Energy efficiency (EE) calculations.**

The gas products were analyzed online by gas chromatography. The mixture gas flow rate coming out from the cathode flow plate was recorded by a mass flowmeter before entering into GC. The concentrations of the products at catholyte and anolyte were quantified using high-performance liquid chromatography.

As to gas products, the Faradaic efficiency ($FE_i$) was calculated by the following equation:

$$FE_i = Z \times F \times f_i/(I \times V_m) \quad (1)$$

As to liquid products, the Faradaic efficiency ($FE_i$) was calculated by the following equation:

$$FE_i = Z \times F \times \left(V_{iC} \times n_{iC} + V_{iA} \times n_{iC}\right)/(I \times t) \quad (2)$$

The energy efficiency ($EE_i$) of every product is calculated by the following equation:

$$EE_i = (1.23\ V - E_{i\ vs\ NHE}) \times FE_i/E_{Vcell} \quad (3)$$

The total energy efficiency of the cell is calculated by the following equation:

$$EE_{Total} = \sum EE_i \quad (4)$$

$Z$ represents the number of electrons needed to produce a mole of *i*, and $F$ represents Faradaic constant, 96485 C mol$^{-1}$. $I$ represents the applied current, A. $V_m$ represents molar volume, 22.4 L mol$^{-1}$. $f_i$ represents volume flow rate, L h$^{-1}$.$t$ represents the time of the applied current, s. $V_{iC/A}$ represents the volume of catholyte and anolyte measured by calculating the difference between the collecting bottle before and after experiments, L. $n_{iC/A}$ represents the concentration of product $i$ in catholyte and anolyte measured by liquid chromatography, mol L$^{-1}$.

| Main Products | Reactions | ΔG(kJ/mol) | $E_{i\ vs\ NHE}$ (V) |
|---|---|---|---|
| Carbon monoxide | $CO_2 \rightarrow CO+0.5\ O_2$ | 257.22 | -0.106 |
| Methane | $CO_2+2\ H_2O \rightarrow CH_4+2\ O_2$ | 818.11 | 0.169 |
| Formic acid | $CO_2+\ H_2O \rightarrow CH_2O_2+0.5\ O_2$ | 269.87 | -0.17 |
| Ethylene | $2\ CO_2+2\ H_2O \rightarrow C_2H_4+3\ O_2$ | 1331.3 | 0.078 |
| Ethanol | $2\ CO_2+3\ H_2O \rightarrow C_2H_6O+3\ O_2$ | 1325.44 | 0.084 |
| Acetic acid | $2\ CO_2+2\ H_2O \rightarrow C_2H_4O_2+2\ O_2$ | 873.52 | 0.1 |
| Propionic acid | $3\ CO_2+3\ H_2O \rightarrow C_3H_6O_2+3.5\ O_2$ | 1509.95 | 0.11 |
| Propionaldehyde | $3\ CO_2+3\ H_2O \rightarrow C_3H_6O+4\ O_2$ | 1767.93 | 0.08 |
| Isopropanol | $3\ CO_2+4\ H_2O \rightarrow C_3H_8O+4.5\ O_2$ | 1951.00 | 0.09 |

**COMSOL Multiphysics simulations.**

***Model development***

The MEA model comprises a 50 μm anion-exchange membrane (AEM), a 5 μm Cu cathode catalyst layer (CL), and a 50 μm film, as shown below.[3] The settings come from previous report MEA.[3-5]


***Charge transfer kinetics***

The oxygen evolution reaction (OER) at the anode:

$$2OH^- \rightarrow O_2 + 2H_2O + 4e^-$$

The hydrogen evolution reaction (HER) and $CO_2$RR reactions occur at the Cu cathode. The following cathodic reactions are considered:

$$2H_2O + 2e^- \rightarrow H_2 + 2OH^-$$

$$CO_2 + H_2O + 2e^- \rightarrow CO + 2OH^-$$

$$CO_2 + H_2O + 2e^- \rightarrow HCOO^- + OH^-$$

$$CO_2 + 6H_2O + 2e^- \rightarrow CH_4 + 8OH^-$$

$$2CO_2 + 8H_2O + 12e^- \rightarrow C_2H_4 + 12OH^-$$

$$2CO_2 + 9H_2O + 12e^- \rightarrow C_2H_5OH + 12OH^-$$

$$3CO_2 + 13H_2O + 18e^- \rightarrow C_3H_7OH + 8OH^-$$

The partial current density of product k is described by the concentration-dependent kinetics:

$$i_{loc,expr} = i_0\left(C_R exp\left(\frac{\alpha_a F\eta}{RT} - C_O exp\left(\frac{-\alpha_c F\eta}{RT}\right)\right)\right)$$

$i_0$ is the exchange current density; $\alpha_a$ is the anodic transfer coefficient; $\alpha_c$ is the cathodic transfer coefficient, $C_R$ is the reduced species expression; $C_O$ is the oxygen reactant expression.

***Carbonate equilibria***

$CO_2$, $CO_3^{2-}$, $HCO_3^-$, $OH^-$, $H^+$, and $H_2O$ are all in equilibrium:

$$CO_2 + OH^- \leftrightarrow HCO_3^- \qquad K_1$$

$$HCO_3^- + OH^- \leftrightarrow CO_3^{2-} + H_2O \quad K_2$$

$$H_2O \leftrightarrow H^+ + OH^- \qquad K_3$$

***Species transport***

The species transport in the various layer is given by the Nernst-Plank equations:

$$N_i = -D_i\nabla c_i - z_j u_{m,i} F c_i \nabla\emptyset_l + c_i u$$

$D_i$ is the diffusion coefficient, $c_i$ is the concentration of *i* ion; $z_j$ is the number of electrons in reaction *j*, $u_{m,i}$ is the mobility, $F$ is Faraday's constant, $\emptyset_l$ is the electrolyte potential.

**Table S1** The parameters used for the simulation.[3,4]

| Parameters | Value | Parameters | Value |
|---|---|---|---|

| | | | |
|---|---|---|---|
| a_C2H4 0.67 | 0.67 | i0_C3H7OH | 4.9e-9 [mA $cm^{-2}$] |
| a_C2H5OH | 0.74 | i0_CO | 2.6 [mA $cm^{-2}$] |
| a_C3H7OH | 0.75 | i0_H2 | 1e-2 [mA $cm^{-2}$] |
| a_CO | 0.17 | i0_HCOO | 2.2e-1 [mA $cm^{-2}$] |
| a_H2 | 0.28 | i0a_O2 | 1.6e-6 [mA $cm^{-2}$] |
| a_HCOO | 0.37 | Th | 5 [um] |
| C_CO2 | 23.9 [mM] | y_CO2_C2H4 | 1.36 |
| D_CO2 | $1.910*10^5$ [$cm^2*s^{-1}$] | y_CO2_C2H5OH | 0.96 |
| D_CO3 | $0.923*10^5$ [ $cm^2*s^{-1}$] | y_CO2_C3H6O | 0.96 |
| D_H | $9.311*10^5$ [ $cm^2*s^{-1}$] | y_CO2_C3H7OH | 0.96 |
| D_HCO3 | $1.185*10^5$ [ $cm^2*s^{-1}$] | y_CO2_CH4 | 0.84 |
| D_OH | $5.293*10^5$ [ $cm^2*s^{-1}$] | y_CO2_CO | 1.5 |
| film | 50 [um] | y_CO2_H2 | 0 |
| i0_C2H4 | 1.9e-6 [mA $cm^{-2}$] | y_CO2_HCOO | 2 |
| i0_C2H5OH | 1.2e-8 [mA $cm^{-2}$] | | |

**The coverage calculation**

In this work, all the DFT calculations were carried out with periodic slab models using the Vienna ab initio simulation program (VASP) with DFT-D3 empirical van der Waals attraction corrections.[6-8] The generalized gradient approximation was used with the PBE exchange-correlation functional.[9] The description of the electron-ion interactions was supported by the projector-augmented wave (PAW) method.[10] The cut-off energy for the plane-wave basis set was 500 eV. We employed (4×4×4) FCC Cu (111) crystal surface to construct the adsorption model for subsequent calculations. The coverage criteria for energies and forces were set to $10^{-5}$ eV and 0.02 eV/Å. The first order Methfessel-Paxton method with a smearing width of 0.1 eV was used. In any slab model, at least a 15 Å vacuum layer is introduced to eliminate interactions.

**PV-driven MEA $CO_2$ reduction system and solar-to-fuel efficiency calculation**

PV–EC system was contrasted by coupling a $CO_2$RR MEA electrolyzer with a three junction $GaInP_2$/InGaAs/Ge photovoltaic to supply power for $CO_2$ reduction under renewable solar energy to access its feasibility in practice.[11] InGaAs/$GaInP_2$/Ge obtained from Shanghai Fullsuns Technology Co., Ltd. In this device, the prepared Cu and the optimized Ni net/NF served as the cathode and anode, separately. All sets of electrolyzer are just as in the test above. Gas product was analyzed online. Liquid products were collected and analyzed.

Energy efficiency calculation:

$$\eta_i = n_i \times \triangle G_i \times 100 \,/\, P \times A$$

$$\eta_{STF} = \sum \eta_i$$

$n_i$ is the moles of product *i* during a period, $\triangle G_i$ is the Gibbs energy of reaction to produce *i*, P, and A corresponding to illumination intensity and area of the solar cell.

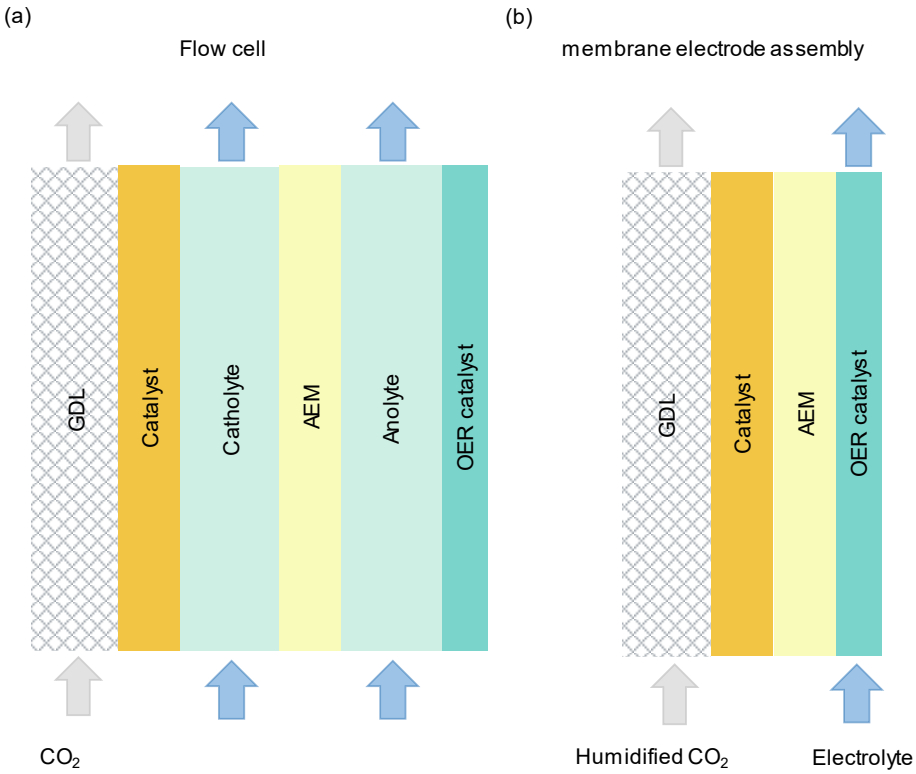


**Fig. S1.** Schematic diagram of the electrochemical $CO_2$ reactor based on the gas-diffusion electrode. (a) flow cell and (b) membrane electrode assembly (MEA).

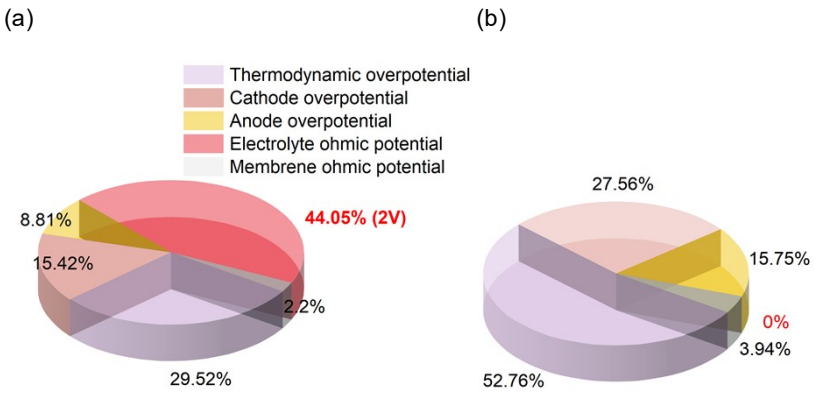


**Fig. S2.** The voltage distribution for (a) flow cell and (b) MEA at 100 mA $cm^{-2}$.

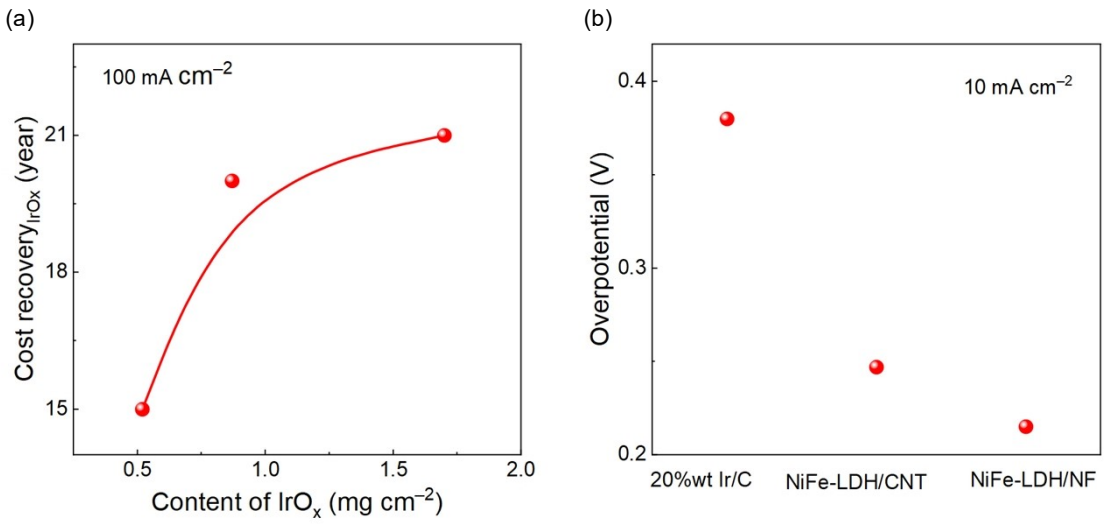


**Fig. S3 (a)** The cost recovery time using different contents of $IrO_x$ as an anode at 100 mA cm$^{-2}$.[12] (b) The overpotential of 20%wt Ir/C, NiFe-LDH/CNT, and NiFe-LDH/NF at 10 mA cm$^{-2}$.[1,13,14]

(a) (b)

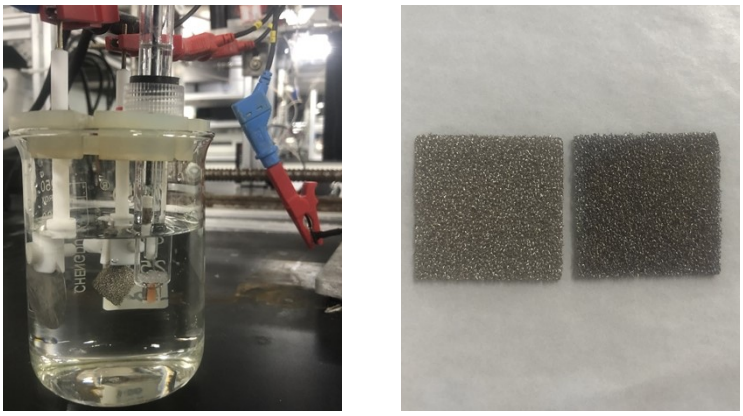

**Fig. S4.** (a) The practical image to prepare electrodeposition. (b) Ni foam (NF) before and after electrodeposition

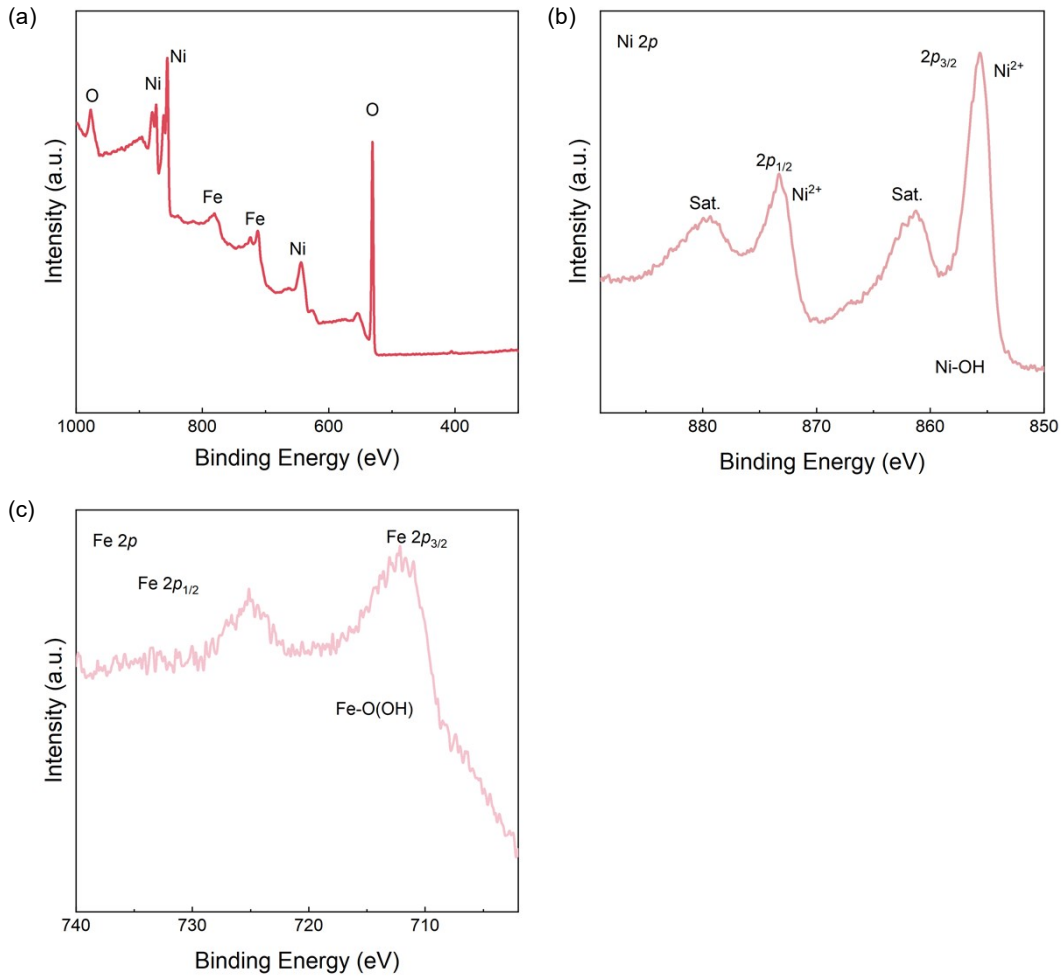


**Fig. S5.** (a) XPS survey spectra of the $NiFeO_x$ composites deposited on Ni foam. (b) and (c) High-resolution XPS of Ni 2p and Fe 2p, respectively. The wide scanning XPS spectrum of the prepared samples reveals the co-existence of Ni, Fe, and O elements (Fig. S5a). The fine-scanning Ni 2p spectrum consists of two spin-orbit doublets of Ni $2p_{3/2}$ (855.643 eV) and Ni $2p_{1/2}$ (873.243 eV), and two satellites (abbreviated as ''Sat.''), which means it is $Ni^{2+}$ oxidation state. No $Ni^0$ was detected, which means that the thickness by electrodeposition is greater than that detected by XPS, otherwise, $Ni^0$ would be detected (The oxidized Ni on the substrate has been removed by 5M HCl). The observation of Fe $2p_{1/2}$ and Fe $2p_{3/2}$ at 724.843 eV and 711.843 eV confirms that Fe is mostly in the $Fe^{3+}$ oxidation state in the composite. The atomic ratio of Ni and Fe in the composite deposited is determined to be 2.7 by XPS. Hence, the $NiFeO_x$ composite obtained is specified as $Ni_{2.7}Fe(OH)_{7.6}$.

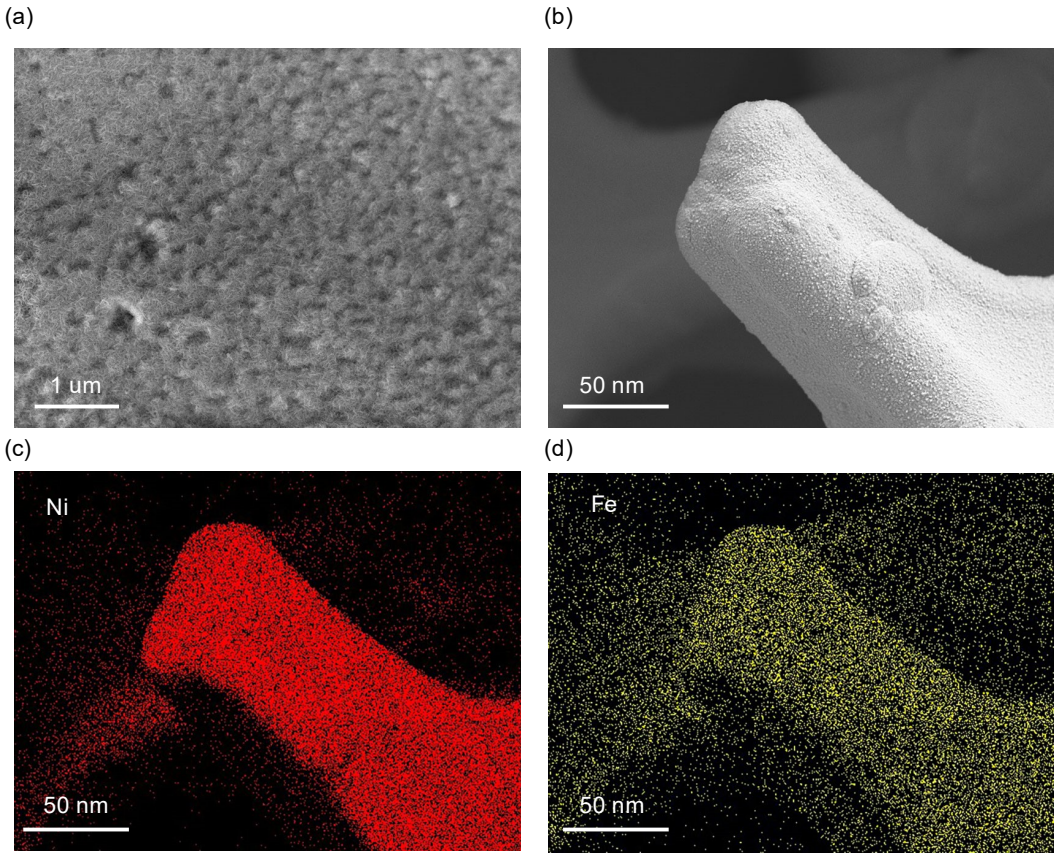


**Fig. S6.** (a) and (b) SEM images of the prepared NiFe LDH/NF. (c) and (d) EDS mappings of Ni and Fe on NiFe LDH/NF.

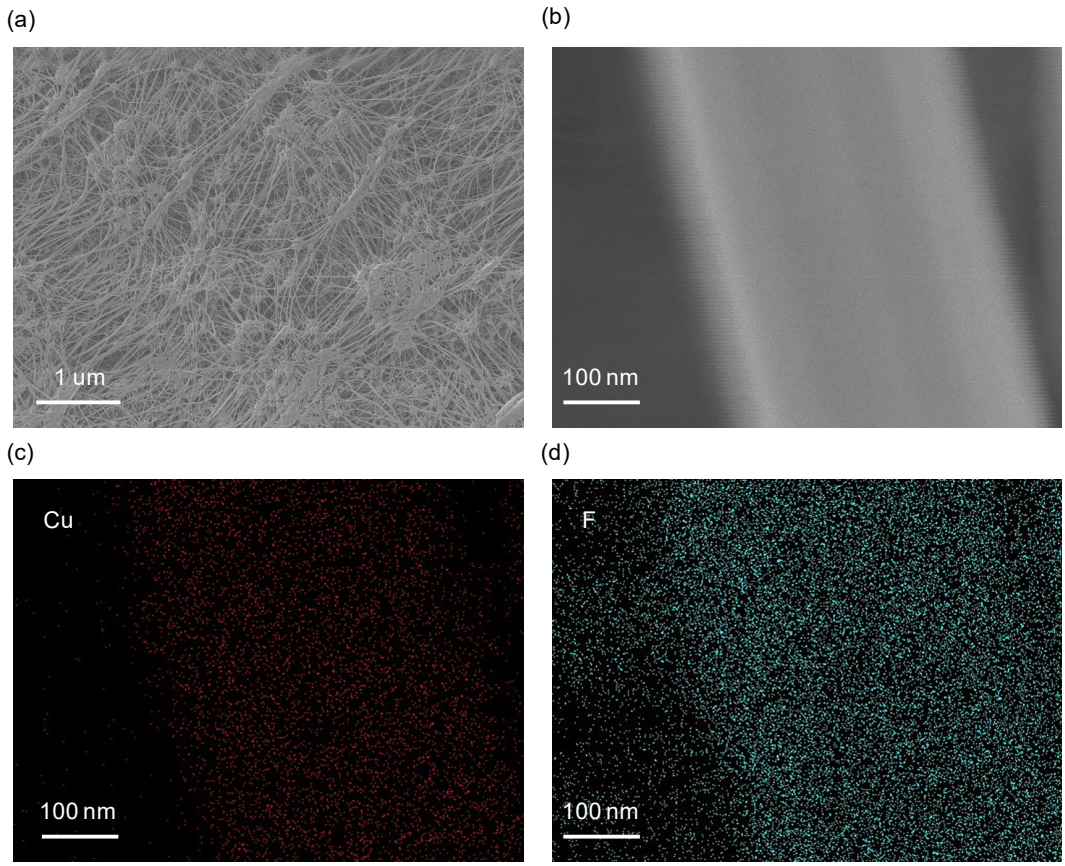


**Fig. S7.** (a) and (b) SEM images of the prepared Cu on GDL. (c) and (d) EDS mapping of Cu and F.

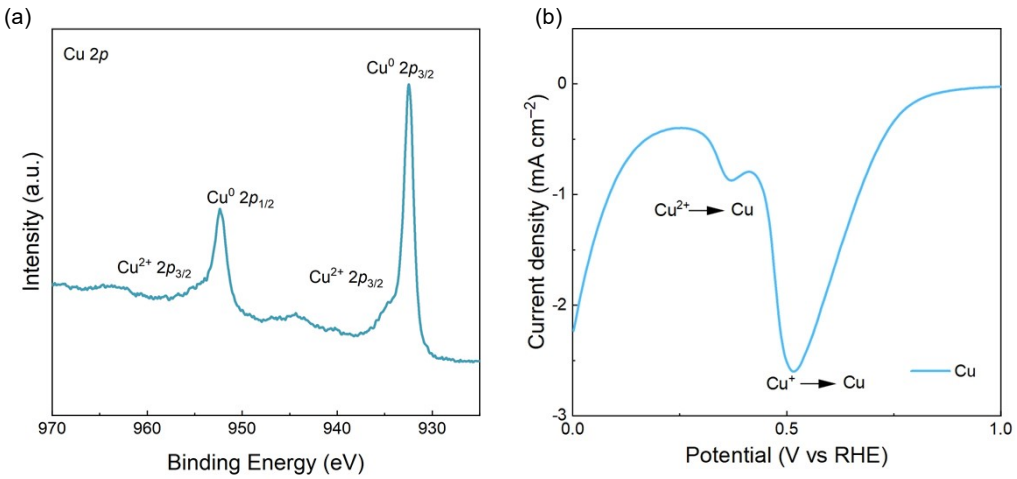


**Fig. S8.** (a) XPS of prepared Cu electrode. (b) LSV of 150 nm Cu in the flow cell in 1M KOH.

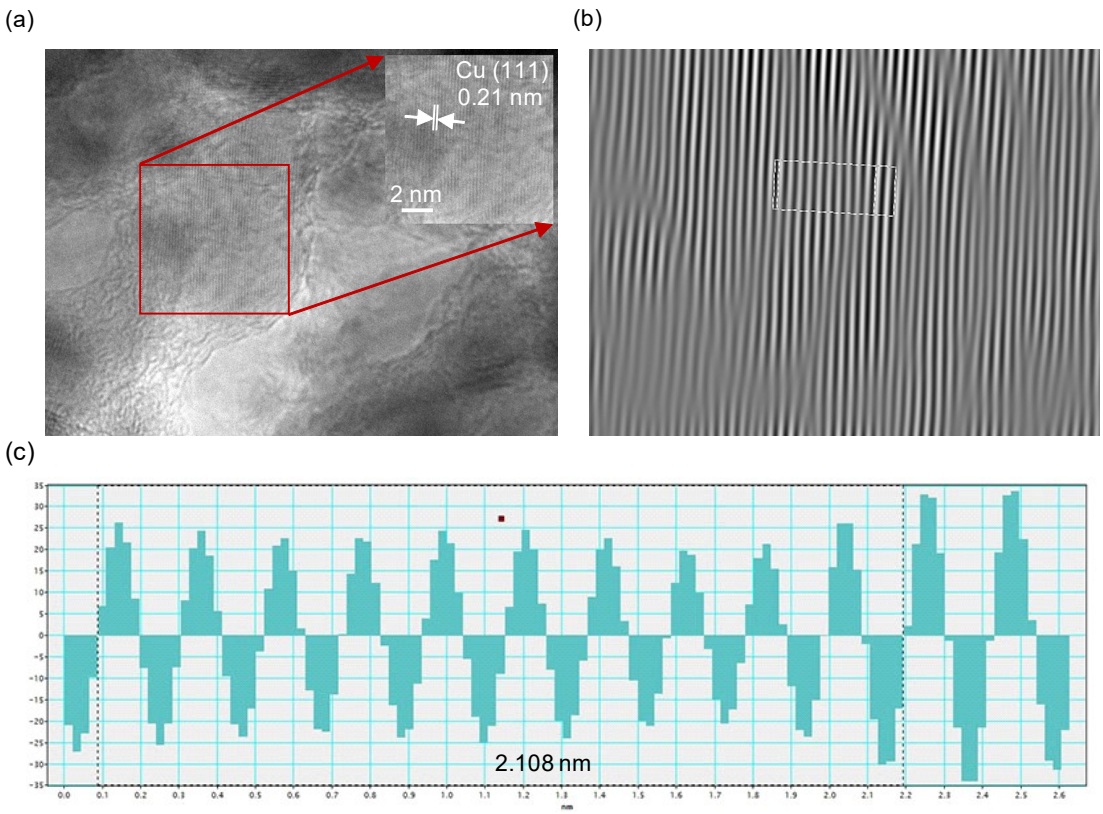


**Fig. S9.** (a) TEM of the prepared Cu. (b) lattice stripes. (c) width of ten lattice stripes.

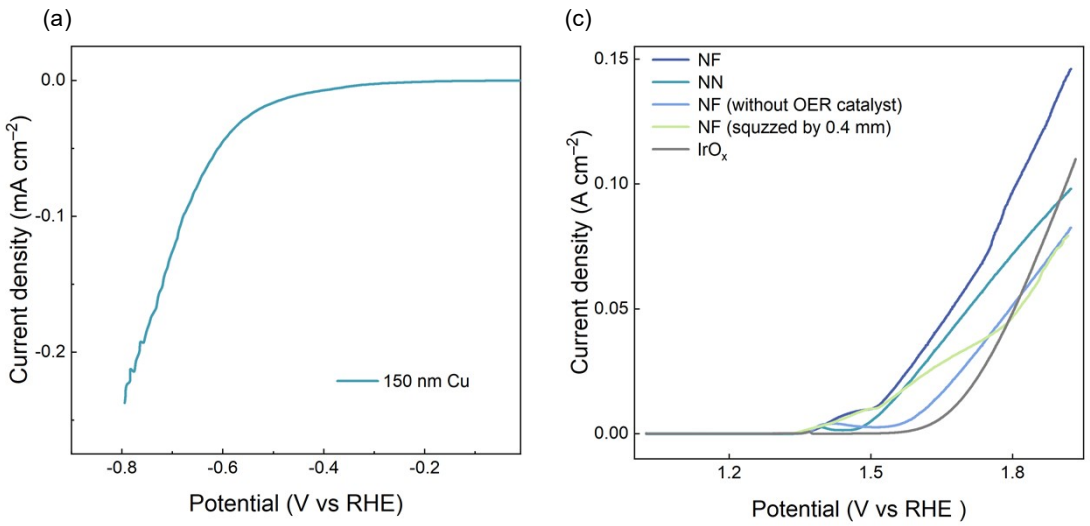


**Fig. S10.** (a) LSV of the prepared 150 nm Cu electrode. (b) LSV of the prepared anode, $IrO_x$, Ni foam (NF), Ni net (NN), Ni foam (without OER catalyst), and Ni foam (compressed by 0.4 mm).

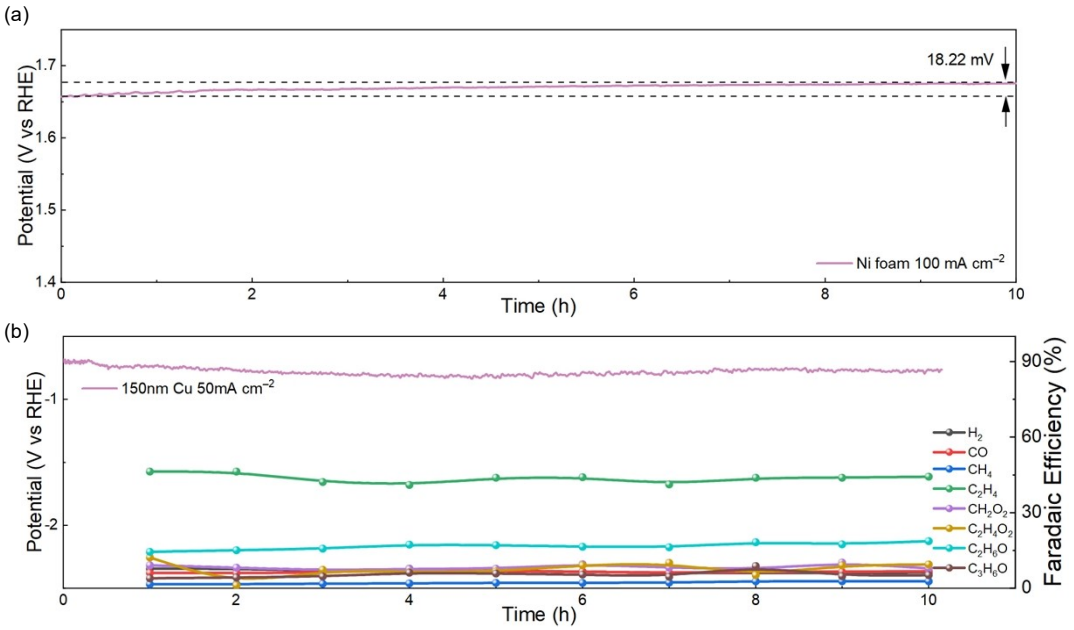


**Fig. S11.** The stability test of (a) anode with 1 cm$^{-2}$ in 100 mL 1M KOH at 100 mA cm$^{-2}$ and (b) cathode with 1M KOH at 50 mA cm$^{-2}$ within 10 h.

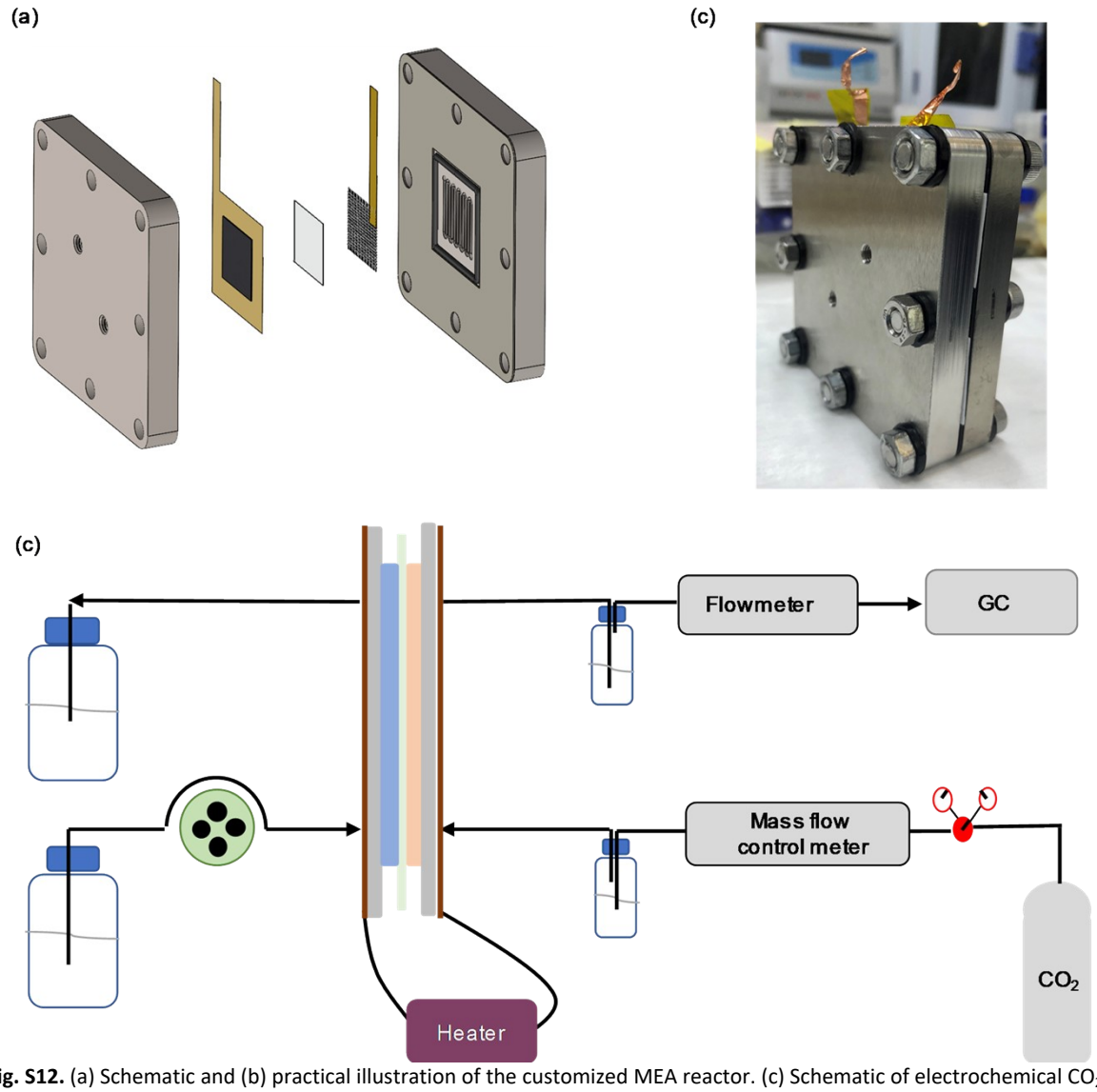


**Fig. S12.** (a) Schematic and (b) practical illustration of the customized MEA reactor. (c) Schematic of electrochemical $CO_2$ reduction test using MEA reactor.

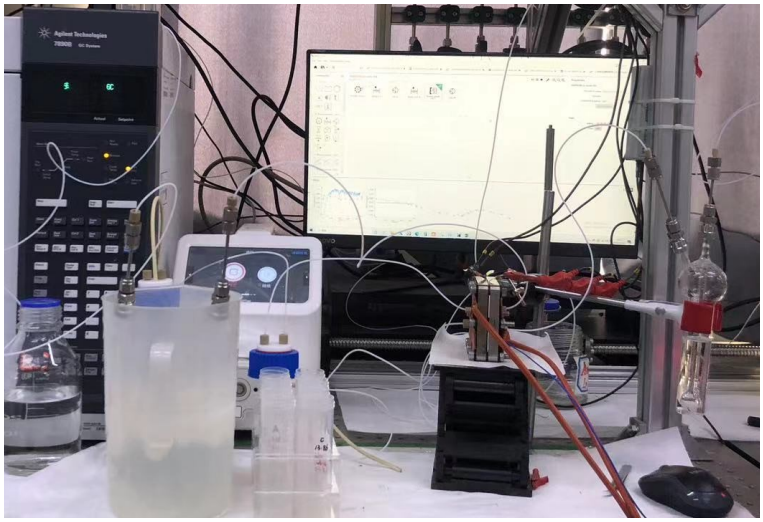

**Fig. S13.** The practical illustration of electrochemical $CO_2$ reduction test using MEA reactor.

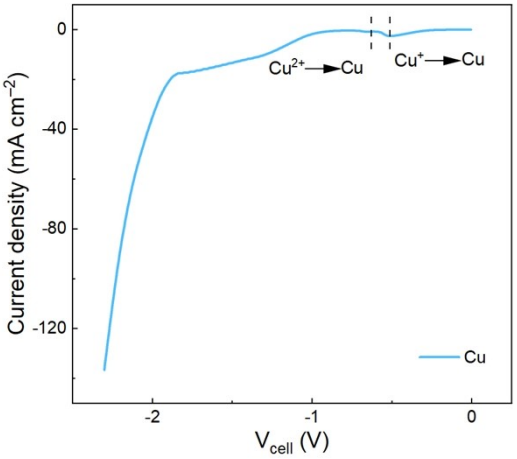


**Fig. S14.** The prereduction of Cu cathode in MEA.

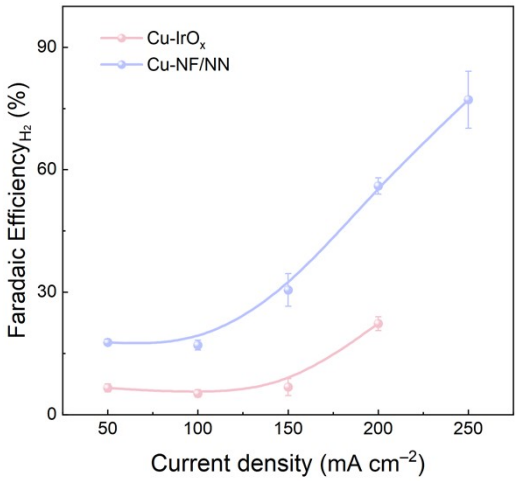


**Fig. S15.** The distribution of the $H_2$ selectivity when using $IrO_x$ and prepared Ni foam/Ni net (NF/NN) anode, respectively.

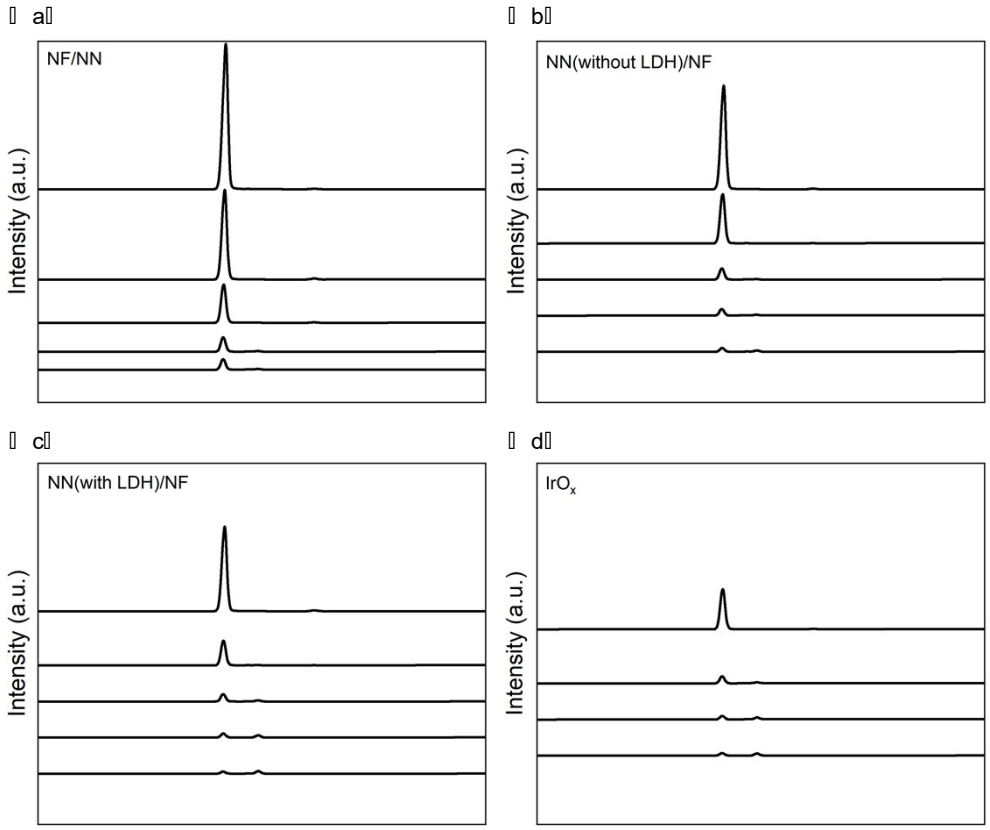


**Fig. S16.** The concentration of the $H_2$ on GC at different current densities for (a) Ni foam/Ni net (NF/NN), (b) Ni net (without LDH)/Ni foam (NN(without LDH))/NF), (c) Ni net(with LDH)/Ni foam (NN(with LDH)/NF), and (d) $IrO_x$.

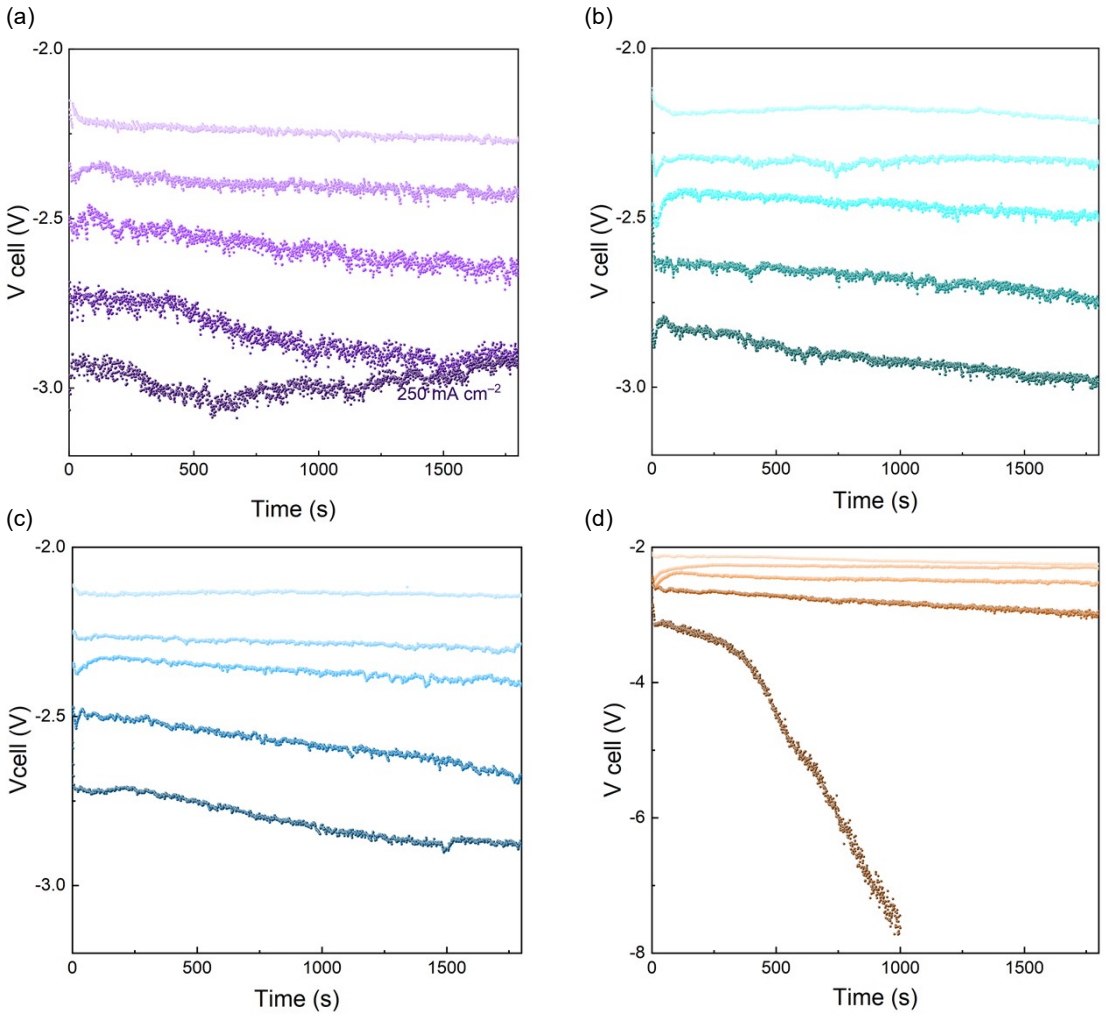


**Fig. S17.** V-t using different anode. (a) Ni foam/Ni net (NF/NN), (b) Ni net (without OER catalyst)/Ni foam (NN (without OER catalyst)/NF), and (c) Ni net (OER catalyst)/Ni foam (NN (OER catalyst)/NF) with a 150 nm Cu cathode. (d) Ni net (OER catalyst)/Ni foam (NN (OER catalyst)/NF) with a 250 nm Cu cathode.

(a) (b)

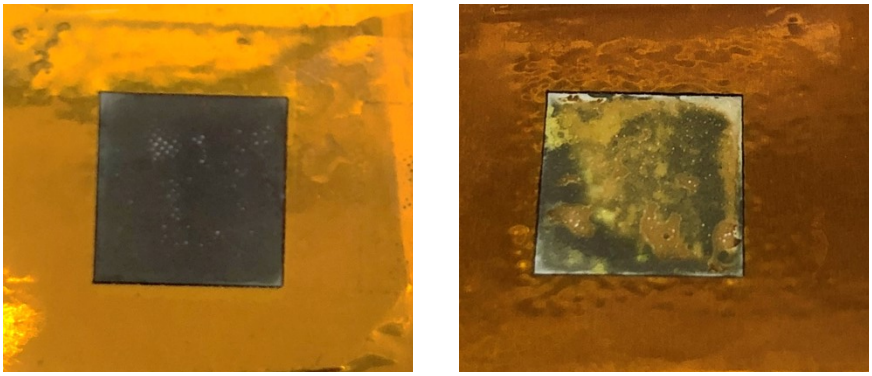

**Fig. S18.** The images of different thicknesses of the Cu electrode after reaction. (a) 150 nm and (b) 250 nm.

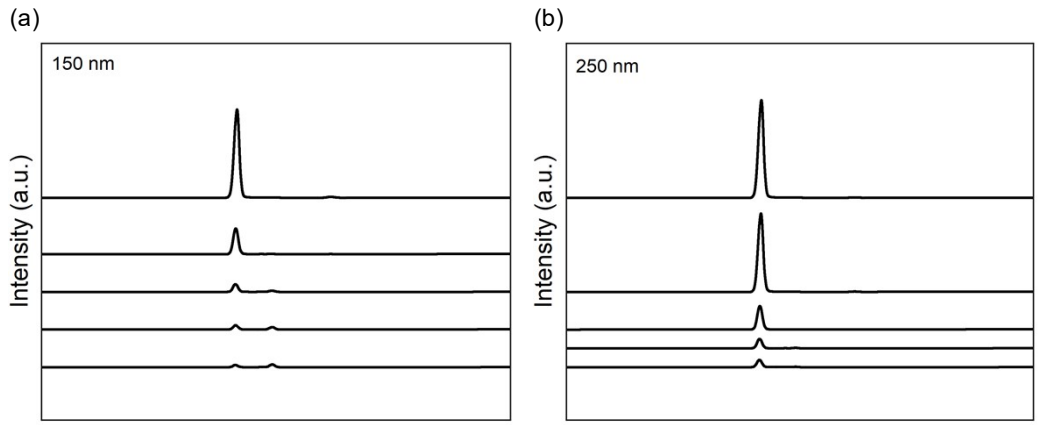


**Fig. S19.** The concentration of the $H_2$ on GC at 50, 100, 150, 200, and 250 mA $cm^{-2}$, for (a) 150 nm and (b) 250 nm of Cu electrode.

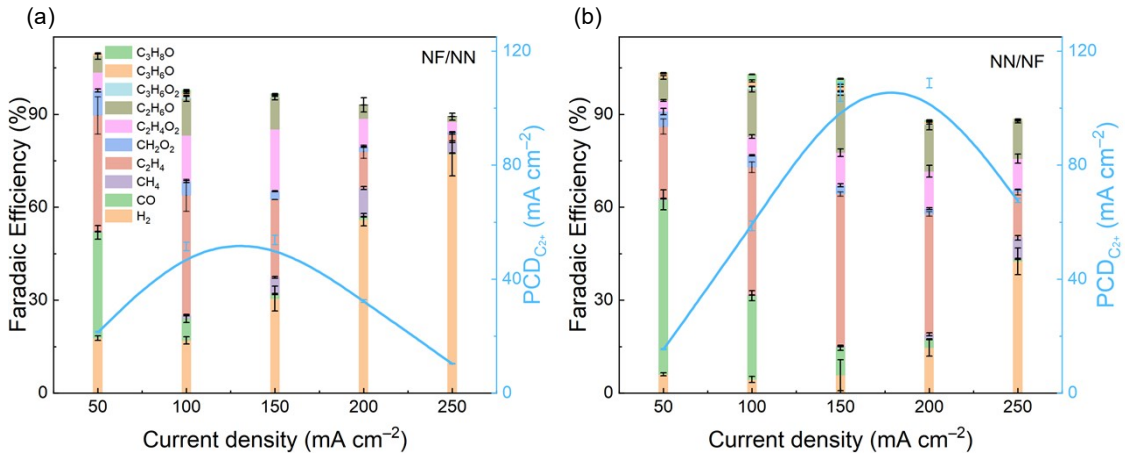


**Fig. S20.** The selectivity of $ECO_2RR$ and partial current density of $C_{2+}$ ($PCD_{C2+}$) using (a) Ni foam/Ni net (NF/NN) and (b) Ni net/Ni foam (NN/NF) as the anode, respectively.

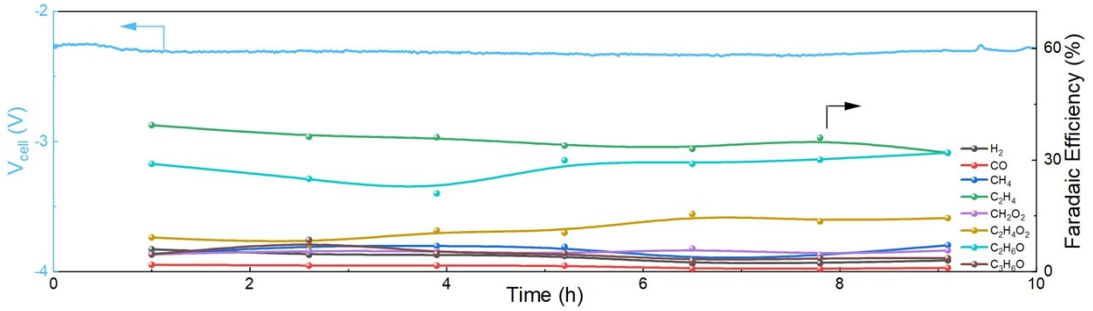


**Fig. S21.** The selectivity distribution of products for the optimized MEA at 100 mA $cm^{-2}$ within 10 h.

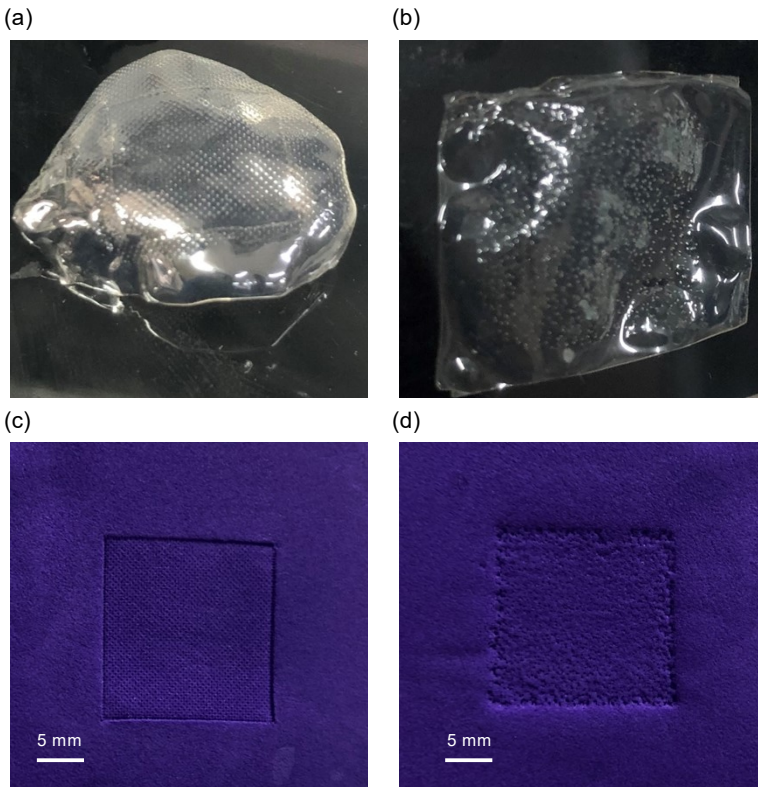


**Fig. S22.** The morphology of the ion exchange membrane after the reaction contacting (a) Ni foam and (b) Ni net, respectively. The reshaping of the contact surface by pressing (c) Ni foam and (d) Ni net onto clay, respectively.

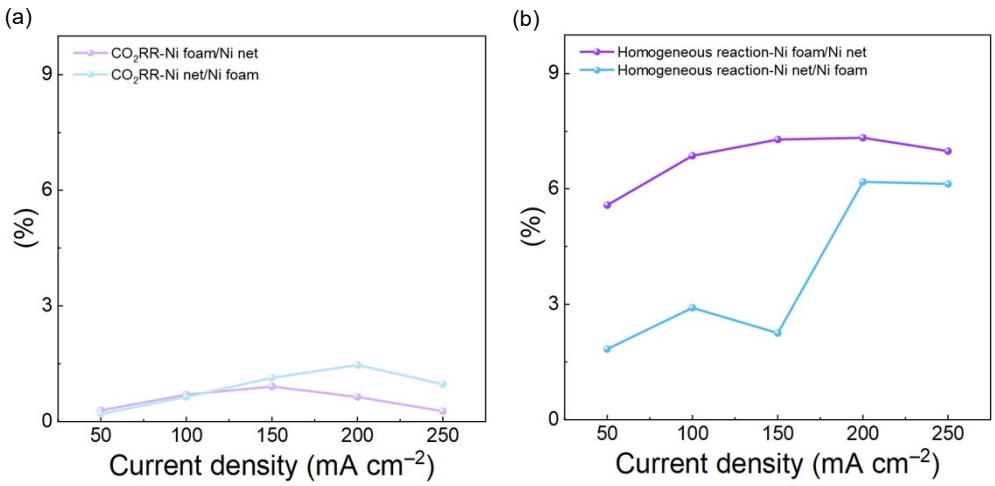


**Fig. S23.** (a) $CO_2$ loss due to $CO_2$RR conversion; (b) $CO_2$ loss due to homogeneous reactions.

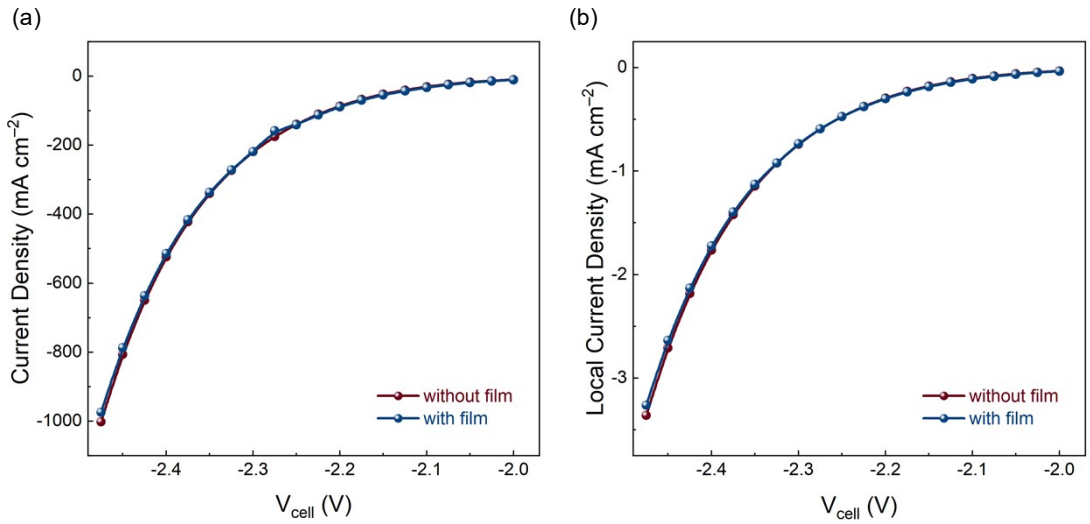


**Fig. S24.** The overall current density (a) and local current density (b) with or without liquid film simulated by COMSOL.

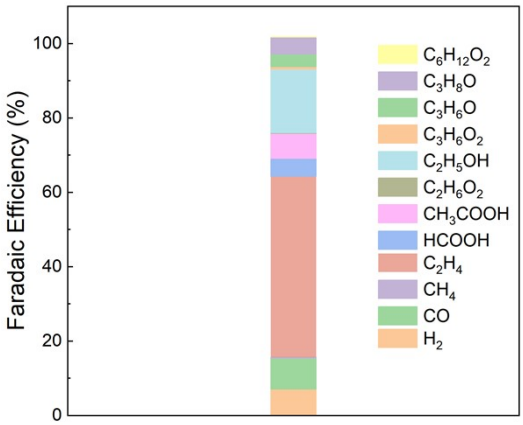


**Fig. S25.** The distribution of $CO_2$RR products when coupling PV with the optimized MEA.

**Table S2.** Recently reported solar to fuel driven by PV.

| Cathode | Anode | Solar to | PV | Ref. |
|---|---|---|---|---|
| Cu (100)-rich film | Ni foam | 4% ($C_2H_4$)<br>6% ($C_{2+}$) | p-n+ Si | [15] |
| CuAg | $IrO_2$ | 4.2% ($C_2H_4$) | Perovskite solar cell | [16] |
| CuO | CuO | 1.93% ($C_2H_4$)<br>2.3% ($C_{2+}$) | Perovskite solar cell | [17] |
| Ag-supported Cu | $IrO_2$ | 1.5% ($C_{2+}$) | Perovskite solar cell | [18] |
| GB-Cu | Se-$(NiCo)S_x/(OH)_x$ | 3.88% ($C_{2+}$) | Si | [19] |
| Cu-Ag | $IrO_2$ | 5% ($C_{2+}$) | Si | [20] |
| PA | $NiO_x$ | 3.1% ($C_{2+}$) | GaInP/GaInAs/Ge | [21] |
| **Cu** | **NiFe LDH** | **6.9 % ($C_2H_4$)**<br>**10.88 % ($C_{2+}$)** | **$GaInP_2$/InGaAs/Ge** | **This work** |

**Reference**


1 X. Lu and C. Zhao, *Nat. Commun.*, 2015, **6**, 6616.
2 W. Luc, J. Rosen and F. Jiao, *Catal. Today*, 2017, **288**, 79-84.
3 L.-C. Weng, A. T. Bell and A. Z. Weber, *Energ. Environ. Sci.*, 2019, **12**, 1950-1968.
4 L.-C. Weng, A. T. Bell and A. Z. Weber, *Energ. Environ. Sci.*, 2020, **13**, 3592-3606.
5 C. M. Gabardo, C. P. O'Brien, J. P. Edwards, C. McCallum, Y. Xu, C.-T. Dinh, J. Li, E. H. Sargent and D. Sinton, *Joule*, 2019, **3**, 2777-2791.
6 G. Kresse and J. Furthmüller, *Comp. Mater. Sci.*, 1996, **6**, 15-50.
7 G. Kresse and J. Furthmüller, *Phys. Rev. B*, 1996, **54**, 11169-11186.
8 S. Grimme, J. Antony, S. Ehrlich and H. Krieg, *J. Chem. Phys.*, 2010, **132**, 154104.
9 J. P. Perdew, K. Burke and M. Ernzerhof, *Phys. Rev. Lett.*, 1996, **77**, 3865-3868.
10 P. E. Blöchl, *Phys. Rev. B*, 1994, **50**, 17953-17979.
11 S. Bai, M. Song, T. Ma, F. Wang, Y. Liu and L. Guo, *Appl. Catal. B.*, 2023, **323**, 122166.
12 P. Mardle, S. Cassegrain, F. Habibzadeh, Z. Shi and S. Holdcroft, *J. Phys. Chem. C.*, 2021, **125**, 25446-25454.
13 Y. Gorlin and T. F. Jaramillo, *J. Am. Chem. Soc.*, 2010, **132**, 13612-13614.
14 M. Gong, Y. Li, H. Wang, Y. Liang, J. Z. Wu, J. Zhou, J. Wang, T. Regier, F. Wei and H. Dai, *J. Am. Chem. Soc.*, 2013, **135**, 8452-8455.
15 G. Zhang, Z.-J. Zhao, D. Cheng, H. Li, J. Yu, Q. Wang, H. Gao, J. Guo, H. Wang, G. A. Ozin, T. Wang and J. Gong, *Nat. Commun.*, 2021, **12**, 5745.
16 J. Gao, H. Zhang, X. Guo, J. Luo, S. M. Zakeeruddin, D. Ren and M. Grätzel, *J. Am. Chem. Soc.*, 2019, **141**, 18704-18714.
17 T. N. Huan, D. A. Dalla Corte, S. Lamaison, D. Karapinar, L. Lutz, N. Menguy, M. Foldyna, S.-H. Turren-Cruz, A. Hagfeldt, F. Bella, M. Fontecave and V. Mougel, *PNAS*, 2019, **116**, 9735-9740.
18 Gurudayal, J. W. Beeman, J. Bullock, H. Wang, J. Eichhorn, C. Towle, A. Javey, F. M. Toma, N. Mathews and J. W. Ager, *Energ. Environ. Sci.*, 2019, **12**, 1068-1077.
19 Z. Chen, T. Wang, B. Liu, D. Cheng, C. Hu, G. Zhang, W. Zhu, H. Wang, Z.-J. Zhao and J. Gong, *J. Am. Chem. Soc.*, 2020, **142**, 6878-6883.
20 Gurudayal, J. Bullock, D. F. Srankó, C. M. Towle, Y. Lum, M. Hettick, M. C. Scott, A. Javey and J. Ager, *Energ. Environ. Sci.*, 2017, **10**, 2222-2230.
21 W.-H. Cheng, M. H. Richter, R. Müller, M. Kelzenberg, S. Yalamanchili, P. R. Jahelka, A. N. Perry, P. C. Wu, R. Saive, F. Dimroth, B. S. Brunschwig, T. Hannappel and H. A. Atwater, *Adv. Energy Mater.*, 2022, **12**, 2201062.